Bayesian inversion of satellite altimetry for Arctic sea ice and snow thickness

Elie René-Bazin[1,2], Michel Tsamados[2], Sabrina Sofea Binti Aliff Raziuddin[2], Joel Perez Ferrer[2], Tudor Suciu[2], Carmen Nab[2,3], Chamkaur Ghag[4], Harry Heorton[2], Rosemary Willatt[2], Jack Landy[5], Matthew Fox[6], and Thomas Bodin[7]

[1]Département de Sciences de la Terre, Ecole Normale Supérieure de Lyon, Lyon, France
[2]Centre for Polar Observation and Modelling, Department of Earth Sciences, University College London, London, UK
[3]Ocean Forecasting Research & Development, Met Office, UK
[4]Department of Physics & Astronomy, University College London, London, UK
[5]Department of Physics and Technology, UiT The Arctic University of Norway, Tromsø, Norway
[6]Department of Earth Sciences, University College London, London, UK
[7]Institute of Marine Sciences (ICM-CSIC), Barcelona, Spain

Correspondence: Elie René-Bazin (elie.rene-bazin@ens-lyon.fr)

Abstract. Inverse methods have been widely used in the field of Earth Sciences, particularly in seismology. Here, we introduce a new application of inversion theory to retrieve Arctic sea ice thickness (SIT) and its overlying snow depth (SD) using freeboard data from the Ku-band radar altimeter CryoSat-2 and the laser altimeter ICESat-2. We do this using the TransTessellate2D algorithm, a Bayesian trans-dimensional approach that allows us to invert for an unknown number of model parameters. This new inverse method is probabilistic in nature, and can offer a novel understanding of covariances between fields of interest as well as their uncertainties. We use this approach to jointly retrieve SIT and SD in one step, without using a climatology for SD. The inversion results demonstrate statistical coherence with snow and ice evaluation products: we obtain a comparable linear regression coefficient and slope to the the AWI CryoSat-2 SD product, when compared to the Operation Ice Bridge (OIB) SD product. Furthermore, our results exhibit similar statistical properties to the UiT and AMSR2 SD products when regressed against this same OIB SD product. For the inverse SIT, the results show good overall agreement with the AWI SIT product, both in terms of spatial patterns and when compared with upward-looking sonar measurements from the Beaufort Gyre Exploration Project moorings. This validation also demonstrates the efficacy of the inverse product in resolving seasonal and interannual anomalies in SIT, as evidenced by its superior correlation coefficient compared to the AWI SIT product. Evaluations against data from MOSAiC and IceBird missions are also promising, particularly for the latter. Using this approach, we can also invert for the altimeter height bias factor from one or both satellites, or potentially in future the evolving sea ice density, in addition to the SIT and SD inversions. This paves the way for future research that constrains such snow and ice height detection biases and improves understanding of their link to SIT and SD retrievals. Lastly, we investigate the multi-frequency inversion using data from the Ka-band SARAL altimeter mission in combination with CryoSat-2, with a view towards the European Space Agency's planned dual-frequency altimetry mission, CRISTAL.

Copyright statement. TEXT

1 Introduction

Over the past decades, climate change has had a significant impact on Earth, especially in the Arctic. In the Arctic Ocean, climate change has induced a decline in September sea ice of $12.8 \pm 2.3\%$ per decade from 1979 to 2018 (Pörtner et al., 2019). Sea ice has a major role in regulating Earth's climate through the exchanges of heat, moisture and momentum between the Arctic Ocean and the atmosphere. Sea ice is also important in regulating the global thermohaline circulation (Stroeve and Notz, 2018). Alongside a declining sea ice extent, the sea ice thickness (SIT) and its overlying snow depth (SD) are thinning. Kwok (2018) found a decrease of 66% in mean SIT at the end of the melt season between 1958-1976 and the CryoSat-2 (2011-2018) period. Such a decrease is also observed for the SD. Webster et al. (2014) found a decrease of $37 \pm 29\%$ for SD in Western Arctic and $56 \pm 33\%$ over the Chukchi Sea between 2009-2013 compared to the Warren climatology (Warren et al., 1999). This climatology corresponds to SD measurements made between 1954-1991 at Soviet stations in the Arctic.

Monitoring SIT over time was only possible with ice-buoys and sonar instruments until the 1990s (Kwok and Rothrock, 2009). Over the last two decades, progress in radar and laser altimetry has made it possible to obtain pan-Arctic spatial and year-round temporal coverage to estimate SIT and SD (Landy et al., 2022). These altimeters measure freeboards, assumed to be the portion of ice (for a Ku-band radar) or ice+snow (for a Ka-band radar or laser) above the sea surface, by measuring the return travel time of the pulse (Armitage and Ridout, 2015).

Despite these improvements, altimeters do have some limitations. Firstly, the coverage depends on the satellite used. CryoSat-2, a Ku-band radar altimeter launched by the European Space Agency in April 2010, can reach 88°N while AltiKa, a radar altimeter using the less common Ka-band microwave band, can only reach 81.49°N. Measurements are made along-track, meaning that several orbits are necessary to obtain sufficient coverage of the Arctic, with standard products given as monthly averages on 25-50 km^2 grids. Recently, novel interpolation algorithms have been developed to compute continuous spatial maps of freeboards from the along-track measurements, on shorter spatio-temporal scales (i.e. daily / 5 km^2) (Gregory et al. (2021), Gregory et al. (2024a)). Another uncertainty comes from the estimation of the freeboard itself. It is commonly assumed that the laser pulse and Ka-band radar are returning from the snow-air interface whereas the Ku-band radar is returning from the snow-ice interface (Laxon et al. (2003), Guerreiro et al. (2016), Lawrence et al. (2018)). However, studies have shown that meteorological and snow geophysical properties could cause the Ku-band radiation to be scattered at levels above the snow/ice interface (e.g., Willatt et al. (2011), Nandan et al. (2017), Nab et al. (2023)). A radar scattering bias that is unaccounted for would introduce a systematic bias in freeboard and derived SIT. Other uncertainties include physical variations in the snow and ice surfaces at footprint level. To take these biases and uncertainties into account, we introduce a bias factor (α), which is the assumed value for the fractional depth of the snowpack from which the laser and radar returns backscatter. If $\alpha = 1$, the pulse is returning from the snow-ice interface (CryoSat-2 default assumption), while for $\alpha = 0$ the pulse is returning from the snow-air interface (default assumption for AltiKa and ICESat-2 (Ice, Cloud and Land Elevation Satellite) Armitage and Ridout (2015)). α is therefore a representation of where the mean scattering horizon resides, independently of the snow thickness.

SIT can be calculated from the freeboards and derived SD under the assumption of hydrostatic equilibrium, using estimates for the ice and snow densities. Zygmuntowska et al. (2014) found that uncertainty in the SD could contribute up to 70% of the total laser altimetry thickness uncertainty. For radar altimetry, Alexandrov et al. (2010) found that the primary cause of error in ice thickness retrieval is uncertainty in sea ice density for thick freeboards (greater than 0.8 m). This uncertainty increases with increasing freeboards. See Landy et al. (2020) for a full uncertainty analysis.

Operational approaches to compute satellite-derived SIT rely on the use of climatological values for SD. The Centre for Polar Observation and Modelling (CPOM; Tilling et al., 2018) and Alfred Wegener Institute (AWI; Hendricks et al., 2023) SIT and volume products are based on CryoSat-2 radar freeboard data (L1B SAR and SARIn mode). The former uses the Warren snow depth climatology (W99; Warren et al., 1999) but with the modification of halving snow depth over first year ice, whilst the latter merges W99 with snow depth estimates from ASMR2 (Rostosky et al., 2018). The NASA product (Petty et al., 2023) uses ICESat-2 laser freeboard (ATL10) data, combined with NASA Eulerian Snow On Sea Ice Model (NESOSIM) snow loading to estimate SIT. These satellite-derived products all use additional auxiliary parameters such as mean sea surface height, sea ice concentration and sea ice type.

Alongside these products, methods have been developed to compute ice and snow thickness directly from multi-sensor approaches. Several studies have suggested utilising co-located satellites to measure dual-frequency freeboards (such as Ku/Ka Band radar or Ku-Band/Laser) to derive SIT and SD (Kwok and Markus, 2017; Kwok et al., 2020; Kacimi and Kwok, 2022). However, this latter approach requires the two satellites to have similar orbits, which is not the case most of the time. Another approach is to use the ratio between SD and SIT (Shi et al., 2020). This method shows promising results but other assumptions are made concerning the thermal state of ice and snow.

Inverse methods have the potential to account for new datasets to derive estimates of SIT while accounting for complexities and uncertainties (Tarantola, 2005). The inversion approach used here allows us to address some of the issues raised previously, namely the prescribed SD or collocation of the satellite data. The 2D trans-dimensional Bayesian method produces a probabilistic solution made of a large ensemble of models for SIT and SD, but also for bias factors (α). With such a trans-dimensional approach, the dimension of the model space (Pan-Arctic SIT, SD and α) is an unknown during the inversion and depends on the density and uncertainty of the input data. The algorithm we use is adapted from the code presented in Hawkins et al. (2019a), previously used to compute contemporary rates of relative sea level change (Hawkins et al., 2019b) and recently adapted for coastal SLR monitoring (Oelsmann et al., 2024). We first introduce the data used and the inversion method, before showing our results with different parametrisations. We compare these results with other SD and SIT products, as well as some *in situ* measurements (BGEP, MOSAiC, IceBird). Finally, we discuss the future evolutions and potential of this method for data fusion of heterogeneous satellite input data in the context of the European Space Agency's (ESA) upcoming dual-frequency polar mission, CRISTAL (Copernicus Polar Ice and Snow Topography Altimeter).

2 Data

The data used for the inversion comes from CryoSat-2 (CS; L1B Baseline E), AltiKa (AK) and ICESat-2 (IS; ATL10 v6; Kwok et al., 2023b). These satellites were launched in 2010, 2013 and 2018, respectively. CS is a Ku-band radar altimeter, AK is a Ka-band radar altimeter and IS is a laser altimeter. We use the Lognormal Altimeter Retracker Model (LARM) processed dataset for CS and AK. This is a physical retracker approach to obtain a more accurate measurement of the freeboard, by incorporating a better understanding of the sea ice's large-scale roughness (Landy et al., 2020).

The inputs for the algorithm are two maps of freeboards from a combination of two satellites (either CS-IS or CS-AK). The input maps are obtained by binning 15 days (15th of the month $\pm$ 7 days) of along-track radar and laser freeboard data onto the 25 km EASE 2.0 grid (Brodzik et al., 2012) for every month considered. Note that the data within the 15-day window are assumed equivalent in time. By using multiple days of data as input (especially with IS where clouds often obstruct data collection) we allow the algorithm to construct more cells. To optimise computational efficiency, the inversion was performed within this interval for each month. Extending the period would increase the volume of input data, thereby lengthening the inversion.

The accuracy of the inversion depends on uncertainties in the component datasets, and the weighting given to each freeboard measurement is based on these uncertainties (e.g. Nab et al. (2025)):

- **CryoSat-2 and AltiKa:** To calculate the freeboard uncertainty for the binned radar freeboard data in each grid cell, we follow the methods of Landy et al. (2024). To start, we calculate the "single shot" range error for each grid cell: $0.1 \cdot (1/\sqrt{N})$ for CS SAR mode and $0.14 \cdot (1/\sqrt{N})$ for CS SARIn mode, based on Wingham et al. (2006), where N is the number of samples in each grid cell. For AK, based on Dettmering et al. (2015) : $0.05 \cdot (1/\sqrt{N})$. The SSHA uncertainty provided with the LARM data is then binned onto the 25 km EASE-2 grid, using the same method as the freeboard data. The range error and binned SSHA uncertainty are then used to calculate the freeboard uncertainty:

$$FB_{unc}^{CS,AK} = \sqrt{(ssha\_unc \cdot \frac{1}{\sqrt{N_{tracks}}})^2 + range\_error^2} \tag{1}$$

  where N_{tracks} is the number of independent tracks used in the binning and $ssha\_unc$ is the binned SSHA uncertainty for each grid cell

- **ICESat-2:** The beam freeboard uncertainty provided with the IS data is binned onto the 25 km EASE-2 grid, using the same method as the freeboard data. The freeboard segment error is then calculated for each grid cell: $beam\_fb\_unc \cdot (1/\sqrt{N})$, where N is the number of samples in each grid cell. The laser freeboard uncertainty is then calculated as:

$$FB_{unc}^{IS} = \sqrt{(ssha\_interpolation\_error \cdot (\frac{1}{\sqrt{N_{tracks}}})^2 + fb\_segment\_error^2} \tag{2}$$

  where N_{tracks} is the number of independent tracks used in the binning and $fb\_segment\_error$ is the binned beam freeboard uncertainty for each grid cell. An assumed value of 0.01 m is used for the SSHA interpolation error.

The calculated uncertainties will be denoted as σ_{CS}, σ_{AK} and σ_{IS} from here on.

We compare the results from our inversion to the following SIT and SD products:

- **AWI:** SIT product from the AWI Helmholtz Centre for Polar and Marine Research (Hendricks et al., 2023). The product is made over the Arctic Ocean for every month from October to April. The input data to compute the SIT is composed of radar measurements from CryoSat-2 and auxiliary data that includes some geophysical parameters (e.g. sea ice concentration, mean surface height).

- **AMSR2:** AMSR2 is a microwave radiometer working at a 89 GHz frequency, which follows AMSRE, that provides data on sea ice concentration, precipitations and other geophysical processes (Rostosky et al., 2018). Here, we use the AMSR2 product for SD.

- **OIB:** The Operation IceBridge campaign is a NASA program, aimed at improving our understanding of the processes occurring in the polar regions. We use the SD and SIT Quick-Look product (Kurtz et al., 2016), recalculated using the same snow, ice and water densities used for the inversion (see Section 3.1 for details of the values). These data were created using measurements from a laser altimeter with a 1 m footprint (and wavelength of 532 nm) and simultaneously a radar altimeter. Assuming that the laser measures the total freeboard (ice freeboard and overlying snow) and that the radar reflects at the snow-ice interface, we can compute the SD and the SIT. The OIB measurements used here were taken in April 2019. The snow depth data are binned onto the 25 km EASE-2 grid.

- **UiT:** Snow depth data derived from ICESat-2 and CryoSat-2, assuming radar bias factors of 0 and 1, respectively, from Landy et al. (2024).

- **MOSAiC**: Expedition conducted between October 2019-2020 by the research icebreaker R/V Polarstern across the central Arctic Ocean (Willatt et al. (2023), Nicolaus et al. (2022)). The data are available via Itkin et al. (2021). We use the Winter months 2019-2020 (from October 2019 to April 2020).

- **IceBird**: SD from airborne radar of the AWI IceBird project. The measurements are based on the multi-sensor airborne data release and are available with Jutila et al. (2021).

3 Methods

3.1 Forward model

The equations used for the forward model are obtained under the assumption of hydrostatic equilibrium (Forsström et al., 2011). They can be written as follows:

$$F_r^{cs} = \frac{\rho_w - \rho_i}{\rho_w} H_i + (1 - \alpha_{cs}\frac{c}{c_s} - \frac{\rho_s}{\rho_w}) H_s \qquad (3)$$

$$F_r^{ak} = \frac{\rho_w - \rho_i}{\rho_w} H_i + (1 - \alpha_{ak} \frac{c}{c_s} - \frac{\rho_s}{\rho_w}) H_s \tag{4}$$

$$F_l^{is} = \frac{\rho_w - \rho_i}{\rho_w} H_i + (1 - \alpha_{is} \frac{c}{c_s} - \frac{\rho_s}{\rho_w}) H_s \tag{5}$$

where F_r^{cs}, F_r^{ak}, and F_l^{is} are the freeboards for CryoSat-2, AltiKa and ICESat-2, and ρ_w, ρ_i and ρ_s are the densities for sea water, sea ice and snow respectively. H_i is the SIT and H_s is the SD. c_s is the velocity of the radar pulse in the snow and c is the velocity in a vacuum. We assume that $\frac{c}{c_s} = 1.28$ (Kwok, 2014). α_{cs}, α_{ak} and α_{is} are the bias factors for CS, AK and IS respectively. We use the sea ice type product from Aaboe et al. (2021) to classify each grid cell as first-year ice (FYI) or multi-year ice (MYI). We then assign sea ice bulk densities of 916.7 and 882 $kg \cdot m^{-3}$ for FYI and MYI, respectively, per Alexandrov et al. (2010). For sea water, we use $\rho_w = 1023\ kg \cdot m^{-3}$ (Wadhams et al., 1992). ρ_s evolves seasonally following Mallett et al. (2020):

$$\rho_s = 6.50M + 274.51 \tag{6}$$

where M is the number of months since October (i.e. $M = 3$ for January).

In order to formulate an inverse problem, we define a data vector **d**. We jointly invert a combination of CS and IS data (or CS and AK data), and define $\mathbf{d} = (\mathbf{d_{cs}}, \mathbf{d_{is}})$, with $\mathbf{d_{cs}} = \{(c_{cs}^k, F_r^{cs,k}), k \in [1, ..., N_{cs}]\}$, and $\mathbf{d_{is}} = \{(c_{is}^k, F_l^{is,k}), k \in [1, ..., N_{is}]\}$, and where c_{cs}^k are the coordinates of data of index k ($c_{cs}^k = (lon_{cs}^k, lat_{cs}^k)$), $F_r^{cs,k}$ the value of the freeboards of index k, and N_{cs} the number of input data for CryoSat-2 (and same for IS).

3.2 Inverse modelling

A linear inverse problem is formulated following Tarantola (2005):

$$\mathbf{d} = \mathbf{G}\mathbf{m} + \epsilon \tag{7}$$

where $\mathbf{m}$ is the unknown model vector, **d** the data vector defined in 3.1, ϵ represents the data errors (i.e. the inability of the model to explain the data), and **G** is the forward model operator.

In order to parametrise the 2D maps of the variables to reconstruct (H_i, H_s and α), we use nodes and a Delaunay triangulation (Hawkins et al., 2019a). Here, the nodes of the Delaunay triangulation are unknown parameters, they are independent of the data locations and will randomly move during the inversion procedure. For our inversion, the vector $\mathbf{m}$ is defined as $\mathbf{m} = (\mathbf{m_{H_i}}, \mathbf{m_{H_s}})$ with (example for H_i) $\mathbf{m_{H_i}} = \{(c_{H_i}^k, H_i^k), k \in [1, ..., n_H]\}$ where $c_{H_i}^k = (lon_{H_i}^k, lat_{H_i}^k)$ are the 2D coordinates of the node associated with index k (Figure 1), H_i^k the value for SIT associated to the node of index k, and n_H the number of nodes. The model vector $\mathbf{m_{H_s}}$ is defined in a similar way. We also invert for the bias factor, and can thus write the vector model $\mathbf{m} = (\mathbf{m_{H_i}}, \mathbf{m_{H_s}})$. The three nodes defining each Delaunay triangle can be linearly interpolated to any point within the

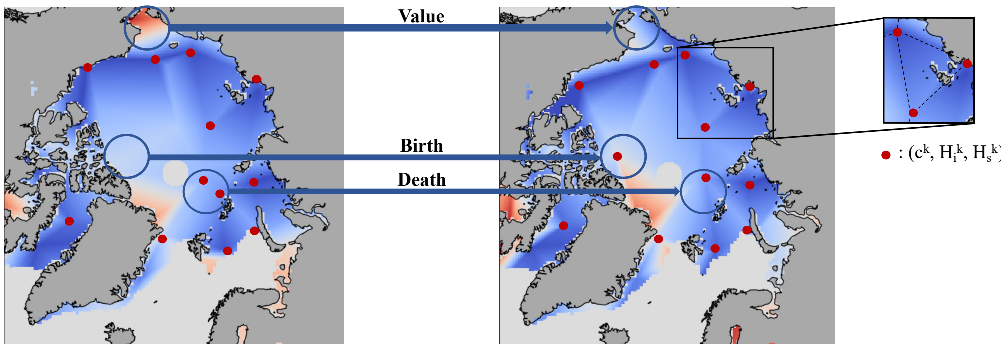

Figure 1. Schematic of 3 of the different perturbations that can be applied at each iteration of the algorithm. We display a zoom on a Delaunay triangle with the different model parameters associated to a node (red point). The red dots are the triangle vertices to which the parameter are associated and the dashed lines are the sides of the triangles. The meaning of each change are **Value** : The value of a randomly chosen node of index k in the map is perturbed as well as its associated values H_i^k and H_s^k ; **Birth** : A new node is created with the associated values randomly drawn from the prior distribution defined previously. That is, a new node is created with position $c_{H_i}^{n_H+1}$, and values $H_i^{n_H+1}$ and $H_s^{n_H+1}$; **Death** : A randomly chosen cell and the associated value of the physical parameter are deleted.

triangle by computing Barycentric coordinates (Sambridge et al., 1995). This then provides a continuous field over the domain but with discontinuities in the gradient at triangle edges.

Here, the dimension of the model space (the number of nodes n_{H_i}) will be treated as an unknown variable to be inverted for. In this way, the level of spatial resolution is directly determined by the data without having to define a smoothing parameter. We summarise the model and data vectors in Table 1.

Inversion name	Satellites	Data space	Model space
CS-IS-2p	CryoSat-2 / ICESat-2	$\mathbf{d_{cs}}, \mathbf{d_{is}}$	$\mathbf{m_{H_i}}, \mathbf{m_{H_s}}$
CS-AK-2p	CryoSat-2 / AltiKa	$\mathbf{d_{cs}}, \mathbf{d_{ak}}$	$\mathbf{m_{H_i}}, \mathbf{m_{H_s}}$

Table 1. Summary table for the setups tested. The data vectors corresponds to the input of the algorithm and the output is a probability distribution in the model space.

In order to recover the model parameters from the observed data, we use a Bayesian approach, where all quantities are defined probabilistically:

$$P(\mathbf{m}|\mathbf{d}) = \frac{P(\mathbf{d}|\mathbf{m})P(\mathbf{m})}{P(\mathbf{d})} \tag{8}$$

where $P(\mathbf{d}|\mathbf{m})$ is the likelihood function representing the probability of observing the data given a particular model, $P(\mathbf{m})$ is the prior probability which represents the information we know on the model before measuring the data **d** (Bodin and Sambridge, 2009) and $P(\mathbf{d})$ can be seen as a normalisation constant. The solution is $P(\mathbf{m}|\mathbf{d})$ and called the posterior probability distribution.

We use uniform prior distributions. For a given model parameter x, the prior distribution is:

$$P(x) = \begin{cases} \frac{1}{b-a}, & \text{if } a \leq x \leq b, \\ 0, & \text{else,} \end{cases} \qquad x \in \{H_i, H_s, \alpha_{cs}, \alpha_{is}\}. \tag{9}$$

The intervals $[a, b]$ for each distribution are as follows:

- H_i: $[0, 6]$ m

- H_s: $[0, 0.5]$ m

The likelihood function is based on a mathematical model for data errors. We make the assumption that the noise on the data is a combination of several sources of uncorrelated errors, such that the final distribution should converge towards a Gaussian as per the Central Limit Theorem. Furthermore, we use diagonal covariance matrices for simplicity (Hawkins et al., 2019a). Thus, the joint likelihood function is a Gaussian likelihood that can be written as

$$P(\mathbf{d}|\mathbf{m}) = P(\mathbf{d_{cs}}, \mathbf{d_{is}}|\mathbf{m}) = P(\mathbf{d_{cs}}|\mathbf{m}) \times P(\mathbf{d_{is}}|\mathbf{m}) = \frac{1}{\sqrt{2\pi}\sigma_{F^r_{cs}}\sigma_{F^l_{is}}} \exp\left(-\frac{\|g(\mathbf{m}) - \mathbf{d_{cs}}\|^2}{2\sigma^2_{F^{cs}_r}} - \frac{\|g(\mathbf{m}) - \mathbf{d_{is}}\|^2}{2\sigma^2_{F^{is}_l}} \right) \tag{10}$$

with $\sigma_{F^{cs}_r}$ and $\sigma_{F^{is}_l}$ being the standard deviations of the input data.

To estimate the posterior solution $P(\mathbf{m}|\mathbf{d})$, we use the reversible-jump algorithm (Green, 1995), which is an extension of the standard McMC Metropolis algorithm to models with variable levels of complexity. The algorithm produces a chain of random Delaunay models where each new proposed model is drawn as a random perturbation of the current model. We note that the range of nodes per model was between 1,000 and 2,000 at the end of the burn-in period (for all the parameters we inverted for). The proposed model is either accepted or rejected according to an acceptance rule based on the ratio of posterior probabilities of the current and proposed models. The solution thus obtained is a large ensemble of Delaunay models representing the posterior distribution.

At each iteration of the random walk, the algorithm makes a random choice between four perturbations of the model parameters (example for inversion of H_i and H_s only):

- **Value:** The value of a randomly chosen node of index k in the map is perturbed as well as its associated values H_i^k and H_s^k .

- **Birth:** A new node is created with the associated values randomly drawn from the prior distribution defined previously. That is, a new node is created with position $c_{H_i}^{n_H+1}$, and values $H_i^{n_H+1}$ and $H_s^{n_H+1}$.

- **Death:** A randomly chosen cell and the associated value of the physical parameter are deleted.

- **Move:** The position of a randomly chosen cell is perturbed (we perturb $c_{H_i}^k$).

These perturbations are illustrated in Figure 1. The random perturbations are drawn from a Gaussian distribution centered on the value of the model parameter and with a specified standard deviation.

We ran the algorithm with 1,500,000 iterations, and removed the first 500,000 models that form the "burn in" stage of the inversion (Brooks et al., 2011). Instead of looking at each of the remaining 1,000,000 models, we compute the mean over the ensemble by taking the average of all sampled values at each pixel. Since individual models have different parameterisations, this results in a smooth continuous map. The standard deviation over the ensemble can also be computed, thus providing a continuous error map. Note that other ways to exploit the information contained in the ensemble are available, such as taking a median, or maximum of the distribution at each geographical location.

3.3 Localised inversion for validation against ULS moorings

The following describes the methods for inversion at a local region, specifically around the upward-looking sonar (ULS) moorings deployed by the Beaufort Gyre Exploration Project (BGEP). The BGEP data were collected at three locations in the Beaufort Sea (BGEP-A, BGEP-B, and BGEP-D) between 2010 and 2024. Sea ice thickness was derived from draft measurements by dividing them by 0.89, as per Rothrock et al. (2003).

In the previous Arctic basin inversion, a 360 × 360 EASE-2 grid was employed. The localised region of interest (ROI) was then defined by cropping this grid to encapsulate each ULS location. We find that a 55 × 55 grid over the Beaufort Sea provides a suitable domain: it fully encompasses each ULS location, avoids placing them near the cropped boundaries, and ensures that the Delaunay triangulation consistently covers the region. For the inversion itself, a 57 × 57 grid is specified. This adds a one-grid point border around the 55 × 55 cropped input, ensuring that no data points are located on the boundaries of the inversion domain.

Since the ROI covers a smaller area than the full Arctic basin, the initial cell count for the inversion could be proportionally reduced. By applying the ratio of the respective grid sizes, this was set to 35 cells. Following the same procedure, the maximum number of cells was derived and rounded to 100. The number of iterations was set through trial and error, and 500,000 iterations were found to be sufficient for the models to stabilise, with the first 100,000 iterations discarded as burn-in. These choices of ROI, cell limits, and iterations reduced the computation time to approximately 10 minutes per day. To verify the robustness of this setup, an ROI inversion was also conducted using the same parameters as the full Arctic inversion (i.e., identical iterations and cell limits). The results were effectively the same as those from the reduced setup, confirming that the lower number of iterations and cells could be used without loss of accuracy. Therefore, the reduced configuration was adopted in order to minimise computation time.

The inversion was then performed at mid-month intervals for the winter periods from 2018 to 2021, corresponding to the years for which comparison data are available from AWI.

4 Results

4.1 Synthetic test

Following standard practice in inversion analyses, synthetic inversions are conducted to assess the validity of the proposed method. Moreover, these experiments provide a basis for comparison with traditional interpolation schemes and serve to illustrate the specific benefits of the inversion framework.

To perform this synthetic test, it is first necessary to produce synthetic data by running the forward model for a given target model. Here we used previously computed fields of SIT and SD to calculate the freeboards, F_l and F_r, by means of Equations 5 and 3. In order to simulate true input freeboards, a random Gaussian noise, but no covariances, is added to the data. Then, we sample the data following a chosen number of orbits tracks and a chosen number of freeboards per track. The data close to the North Pole are removed to simulate true satellite observations.

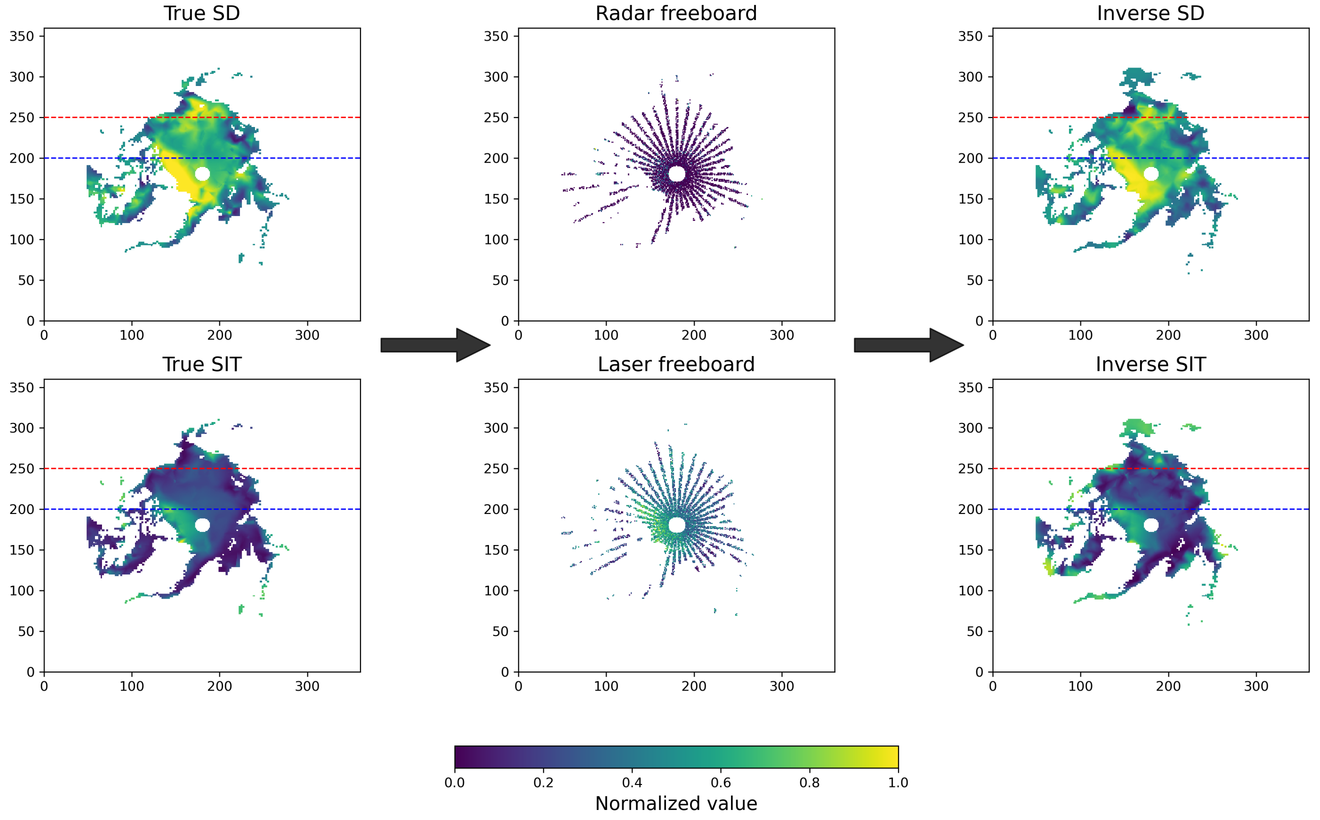

Figure 2. Summary of the synthetic inversion performed. The True SD and SIT fields were previously computed. The values of SIT, SD and freeboards are normalised using the maximum value of each field. The blue and red lines correspond to the lines analysed in Figure 4

Finally, the inversion is carried out using these computed synthetic freeboards as input. The entire procedure is illustrated in Figure 2. It is evident that the retrieved inverse SD and SIT are analogous to the true SD and SIT fields, yet they exhibit a reduced number of features and a smoother aspect in comparison to the original maps. This phenomenon can be attributed to the substantial volume of data utilised in this synthetic evaluation. The true SIT and SD fields were generated following the parametrisation described in Section 2, using 15 days of CS2 and IS2 freeboards (approximately 40,000 measurements), whereas only 9,000 freeboards were used in the synthetic inversion. This reduced dataset was selected to enable faster inversions and allow for multiple synthetic experiments.

The results of this last synthetic test are used as a benchmark to compare to results obtained using a classical interpolation scheme. For this example, we use the GPSat Python library, introduced by Gregory et al. (2024b). No binning of the freeboard data was applied before interpolation, as the synthetic dataset was already defined on a regular grid. The interpolation was performed on a 360×360 grid with a resolution of one grid cell, consistent with the resolution of the synthetic freeboard fields. Prediction locations more than four grid cells away from the nearest observation were excluded to avoid extrapolation. The hyperparameter values were scaled according to those typically used for a 25 km resolution grid: for example, a maximum spatial lengthscale of 600 km (equivalent to 24 grid cells at 25 km resolution) was adapted to 24 grid cells for the 1-grid resolution case. To reduce local noise and ensure spatial continuity, the hyperparameters were additionally smoothed over an 8-grid neighbourhood.

The procedure and the resulting SD and SIT fields are plotted in Figure 3. We first notice that this method uses an additional step compared to the inverse approach, as the freeboards data need first to be interpolated before using the Equations 5 and 3 to compute the SD and SIT and obtain a continuous 2D field. Using the Bayesian inversion approach, this step is not required given the space subdivision effected by the Delaunay triangles. Furthermore, the 'classical' interpolation scheme results in the calculation of a single SD and SIT map only. Conversely, a principal benefit of the Bayesian method is that it enables the calculation of thousands of intermediate models during the inversion process.

In Figure 4a we can see that the distribution of models is close to the true SIT field on an example horizontal transect, that validates the visual observation made with Figure 2. However, in Figure 4c, the shape of the true SIT field is very different from the inverse SIT on a different horizontal transect. These discrepancies between the two studied transects can be explained by the number of input data used. As shown in Figure 2, the number of freeboard data is important for the $\mathbf{y = 200}$ transect as it is close to the North pole. On the other side, for $\mathbf{y = 250}$, the amount of freeboard data is much smaller. Thus, on $\mathbf{y = 200}$ the solution is better constrained by the input data whereas on $\mathbf{y = 250}$, due to the lack of data, the probabilistic solution is wider as a lot of values of SIT are possible. This emphasises the probabilistic nature of the inverse approach introduced here: with a large amount of data, the distribution of models is restricted around the true value whereas with less data the distribution is wider.

This characteristic of the Bayesian approach can also be seen for specific locations as depicted in Figure 4d and Figure 4f. In Figure 4d, the chosen point (red dot) is located close to the North Pole, where the amount of freeboard data is largest. Thus, the distribution of models is restricted around the true value of SIT/SD. However, in Figure 4f, the chosen point is located in a region with fewer freeboard data. As expected, the distribution of models is not centred around the true value. This emphasises

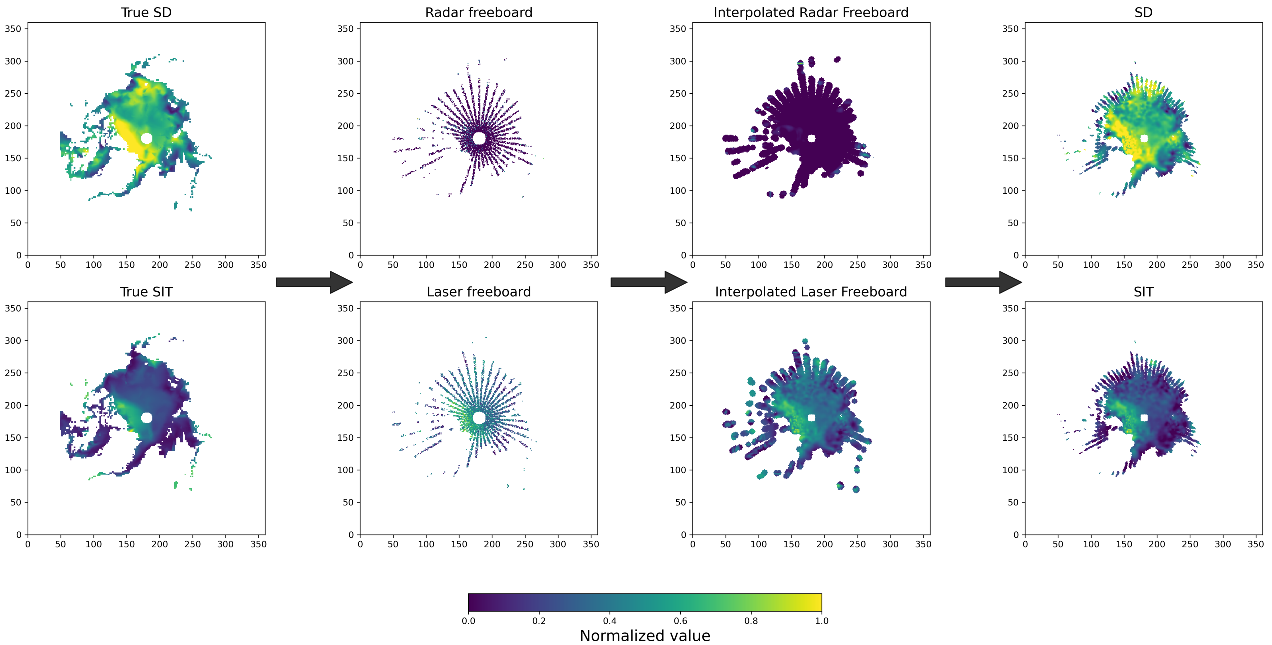

Figure 3. Summary of the procedure used to compute SD and SIT fields using the GPSat interpolation library.

again the fact that, with less input data, the inversion is less constrained and thus the number of possible values for the SIT and SD fields is more important and different from the true value.

Compared to the 'classical' interpolation approach, the Bayesian inversion doesn't produce a single model for the different fields (SIT, SD and any other parameter we would invert for). Instead, it produces a probabilistic solution in which all the models (removing the burn-in period) are of interest (for example to study the behaviour and covariances of the different fields inverted).

Furthermore, this Bayesian approach doesn't require interpolation and can be applied directly to the binned along-track data. These data directly determine the level of smoothing (more data implies more features). With classical methods, the level of smoothing is an arbitrary choice of the user. Instead, with our approach, the level of complexity in the solution is determined by the level of information present in the data.

4.2 Inversion for SIT and SD, with fixed bias factors

Arctic maps of SIT and SD are computed for every winter from 2018 to 2021 using freeboards from a combination of either CryoSat-2/ICESat-2 (CS-IS) or CryoSat-2/AltiKa (CS-AK). The resulting SIT and SD maps are presented in Figures 5 and 8, for prescribed values of $\alpha_{cs} = 1$, $\alpha_{is} = 0$ and $\alpha_{ak} = 0$. The lack of data near the pole for CS-AK is a result of AltiKa's orbit, limited to 81.49°N.

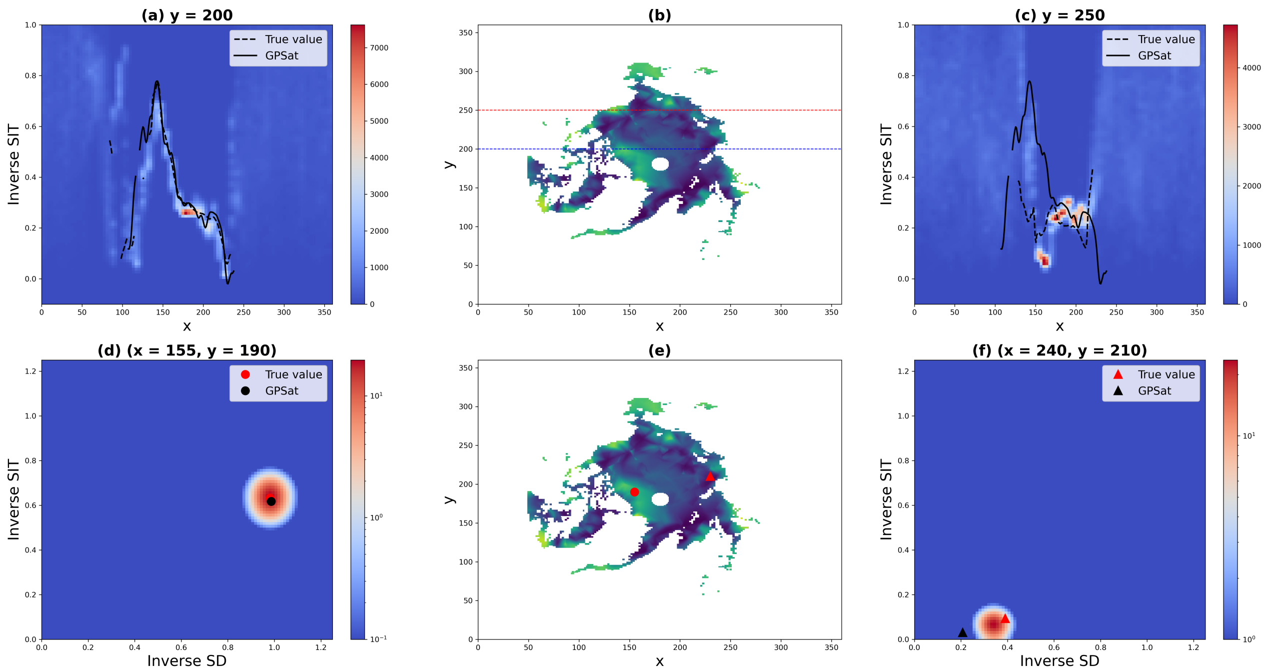

Figure 4. Analysis of the results of the synthetic inversion **(a)** Distribution of the SIT models on the $\mathbf{y = 200}$ horizontal line. The true SIT field is depicted with the black dashed line and the GPSat SIT is depicted with the solid line. **(b)** Inverse SIT map. The horizontal transects used for the analysis are depicted by the blue dashed line for $\mathbf{y = 200}$ and red dashed line for $\mathbf{y = 250}$. **(c)** Distribution of the SIT models on the $\mathbf{y = 250}$ horizontal line. **(d)** Distribution of the SD and SIT models for the pixel ($\mathbf{x = 155}$, $\mathbf{y = 190}$). The results for the True SIT/SD and GPSat are plotted with the red and black respectively. **(e)** Inverse SIT map. **(f)** Distribution of the SD and SIT models for the pixel ($\mathbf{x = 240}$, $\mathbf{y = 210}$).

4.2.1 Sea ice thickness (SIT)

In the CS-IS inversion we observe an increase in SIT from November to April each year. We obtain thicker ice in the North of the Canadian Archipelago and in the Central Arctic (2.5 - 4 m) than in the rest of the Arctic Ocean (0 - 3 m). The CS-AK-2p inversion doesn't include the Central Arctic, but the SIT near the Canadian Archipelago is similar to that found in CS-IS (around 4 m). The observed spatial patterns are consistent with the ice type (MYI or FYI) patterns, with thicker ice found in regions typically dominated by MYI (north of Greenland and Canadian Archipelago). We find similar spatial distributions for the SIT between the two combinations used (CS-IS and CS-AK) which shows that the method appears to be robust and flexible towards the combination of satellites used.

When comparing the results of the inversion to the AWI SIT product, we observe the same spatial patterns for the ice around the Central Arctic. However, the values from the inversion are 0.5 - 1 m higher than the ones from AWI, especially to the north of Greenland. It is worth noting that our inversion results indicate thicker sea ice north of Greenland and in the Canadian Archipelago, while the AWI dataset generally shows greater ice thickness across the broader Arctic Ocean. This result can be confirmed by looking at the maps for AWI (Figure 5, left column) in which we find a wider spread in the thick sea ice over the Arctic Ocean. For the inversion, the thicker sea ice remains contained in a specific area.

Next, we compare the results from the CS-IS model to estimates from airborne sensors retrieved during NASA's Operation Ice Bridge (OIB) campaign in April 2019 (Figure 6).

We find an improved linear correlation coefficient (r = 0.67) and a lower intercept for the inverse solution than the AWI product. The Bias and RMSE are similar for both SIT products (Table 3). The inversion solution underestimates the SIT by 7 cm; however, it represents the spread of thickness estimated by OIB better than the conventional AWI SIT product.

The inverse SIT estimates are further evaluated against BGEP-ULS mooring observations at three locations, using regional inversions performed for each winter season from 2018 to 2021 (see Section 3.3). The corresponding results are presented in Figure 7, and the associated statistics are summarized in Table 2. Overall, the inverse SIT demonstrates performance comparable to that of the AWI product in this validation. As shown in Figure 7, the regression slopes between inverse and AWI SIT are comparable. Notably, the AWI SIT product exhibits values systematically higher by approximately 0.5–1 m across all three ULS sites, compared to the inverse SIT. While the AWI product displays high intercepts (0.15, 0.75 and 0.46 for ULS A, B and D, respectively), the inverse SIT intercept are closer to zero. The inverse approach also yields higher correlation coefficients (r), suggesting an improved ability to capture seasonal and interannual variations in ice thickness. However, the AWI product generally achieves lower bias and RMSE values, except in the comparison with ULS-D.

	Inverse	**AWI**		**Inverse**	**AWI**		**Inverse**	**AWI**
ULS-A			**ULS-B**			**ULS-D**		
Bias	-0.44	-0.12		-0.34	0.23		-0.27	0.26
RMSE	0.49	0.26		0.44	0.43		0.33	0.40
r	0.95	0.90		0.94	0.77		0.96	0.82
Slope	0.67	0.80		0.53	0.62		0.72	0.85
Intercept	-0.02	0.15		0.30	0.75		0.11	0.46

Table 2. Computed statistics corresponding to Figure 7 and the validation of inverse and AWI SIT against the BGEP moorings.

4.2.2 Snow depth (SD)

A main advantage of our method is being able to retrieve ice and snow thickness simultaneously. We retrieve the same spatial patterns for snow between CS-IS and AMSR2, especially over Central Arctic and in the Beaufort Sea (Figure 8). Again, the result with CS-AK is limited because of AltiKa's orbit. Compared to SIT shown in Figure 5, the snow inversion for CS-IS and CS-AK displays larger spatial differences. When looking at the difference between CS-IS and AMSR2, we see that the two snow products are close (the difference being close to zero in a large part of the Arctic Ocean). The most important differences are located in the Beaufort Sea (November 2018) and in the Central Arctic (November 2019 and 2020). The AMSR2 snow depths have a stronger contrast between zones of first-year and multi-year ice, in comparison to the CS-IS SD. We can also

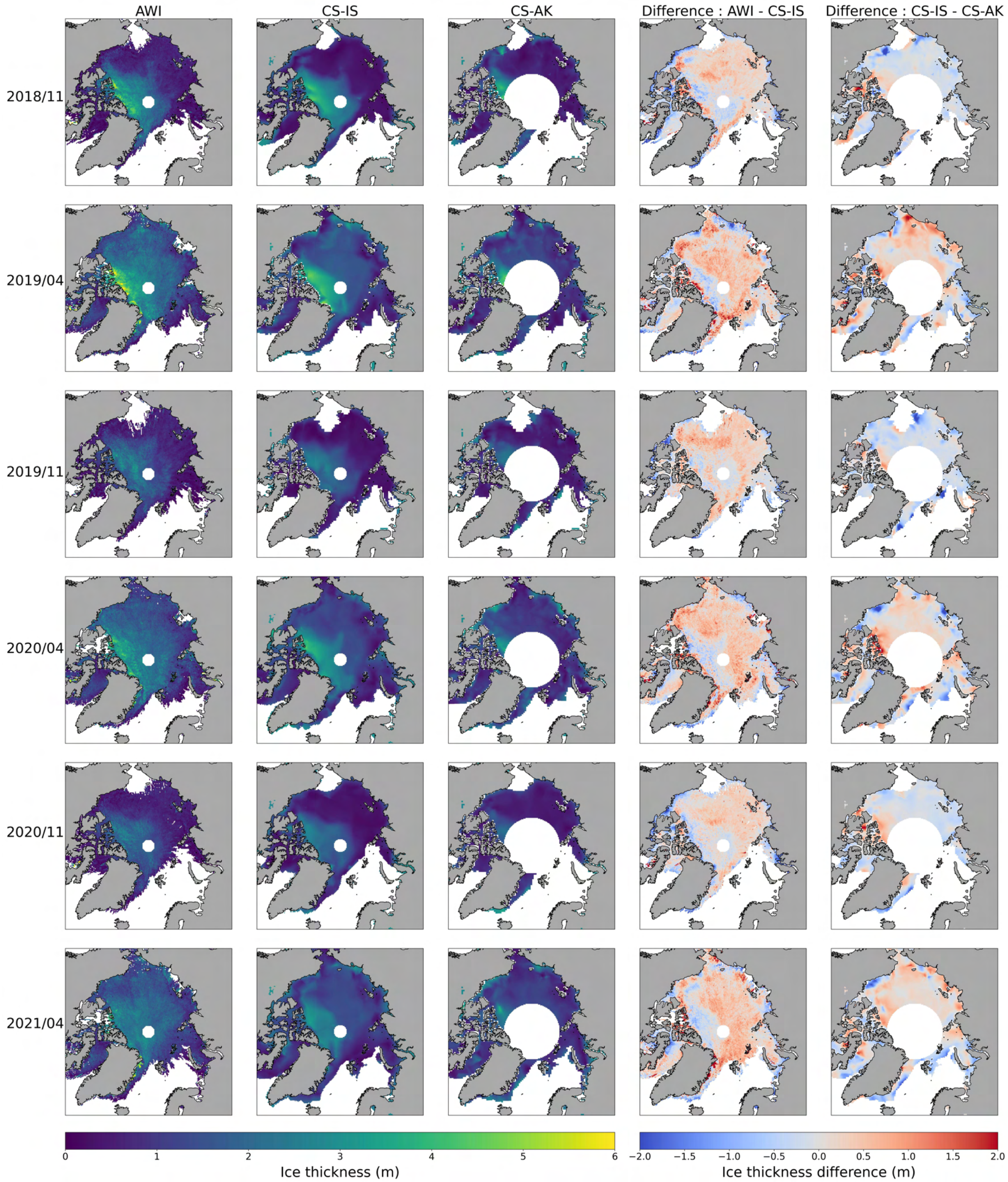

Figure 5. Results of the inversion for SIT using CS-IS-2p and CS-AK-2p, with $\alpha_{cs} = 1$, $\alpha_{is} = 0$ and $\alpha_{ak} = 0$. The first column shows the AWI SIT product, for visual comparison. The second and third columns show the CS-IS and CS-AK results, respectively. The fourth column shows the difference between the AWI product and the CS-IS results. The fifth column shows the difference in inversion results between the two satellite combinations (CS-IS and CS-AK).

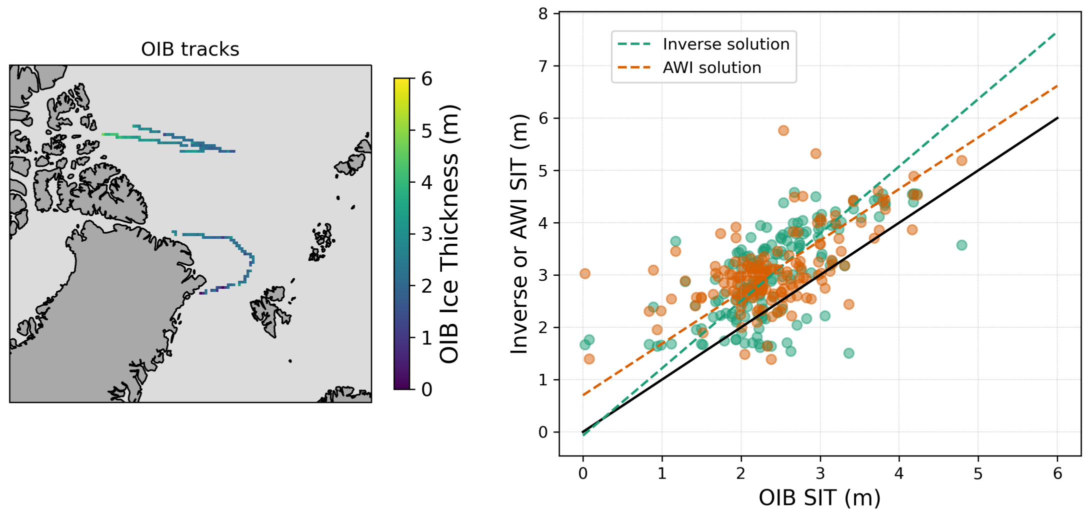

Figure 6. (left) Map of SIT retrieved from OIB tracks for April 2019. (right) Comparison of the CS-IS-2p SIT inversion and AWI SIT product with Operation Ice Bridge for April 2019. The dashed lines of best fit are computed using the orthogonal distance regression between the two sets of data (CS-IS-2p/OIB and AWI/OIB).

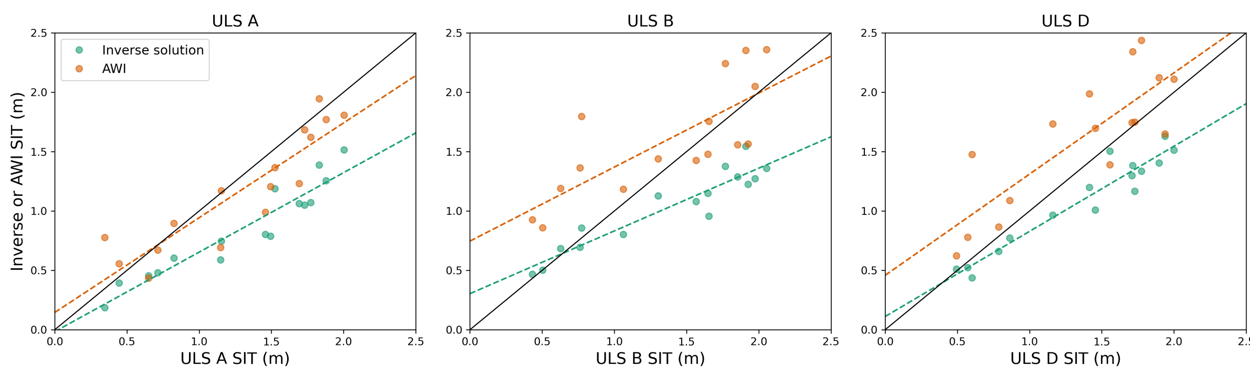

Figure 7. Validation of inverse SIT against BGEP moorings for the winter periods from 2018 to 2021. We also plot the results from AWI.

notice that the differences between CS-IS and AMSR2 are generally higher in November than in April (and for April, the inverse SD is mostly higher than from AMSR2).

Figure 9 and Table 3 show a comparison of the CS-IS-2p inversion results against the OIB, AWI, UiT and AMSR2 SD products. The inversion method produces better results than the AWI product in terms of slope and linear correlation coefficient (r), whereas the bias, RMSE and intercept are similar. The inversion solution tends to overestimate low SD values and underestimate the high ones.

The inverse solution is non-biased ($bias = 0.00$). The UiT product is statistically better than the inverse solution and the AWI product in terms of slope and intercept. Similar values for the bias, RMSE and linear correlation coefficient (r) are obtained

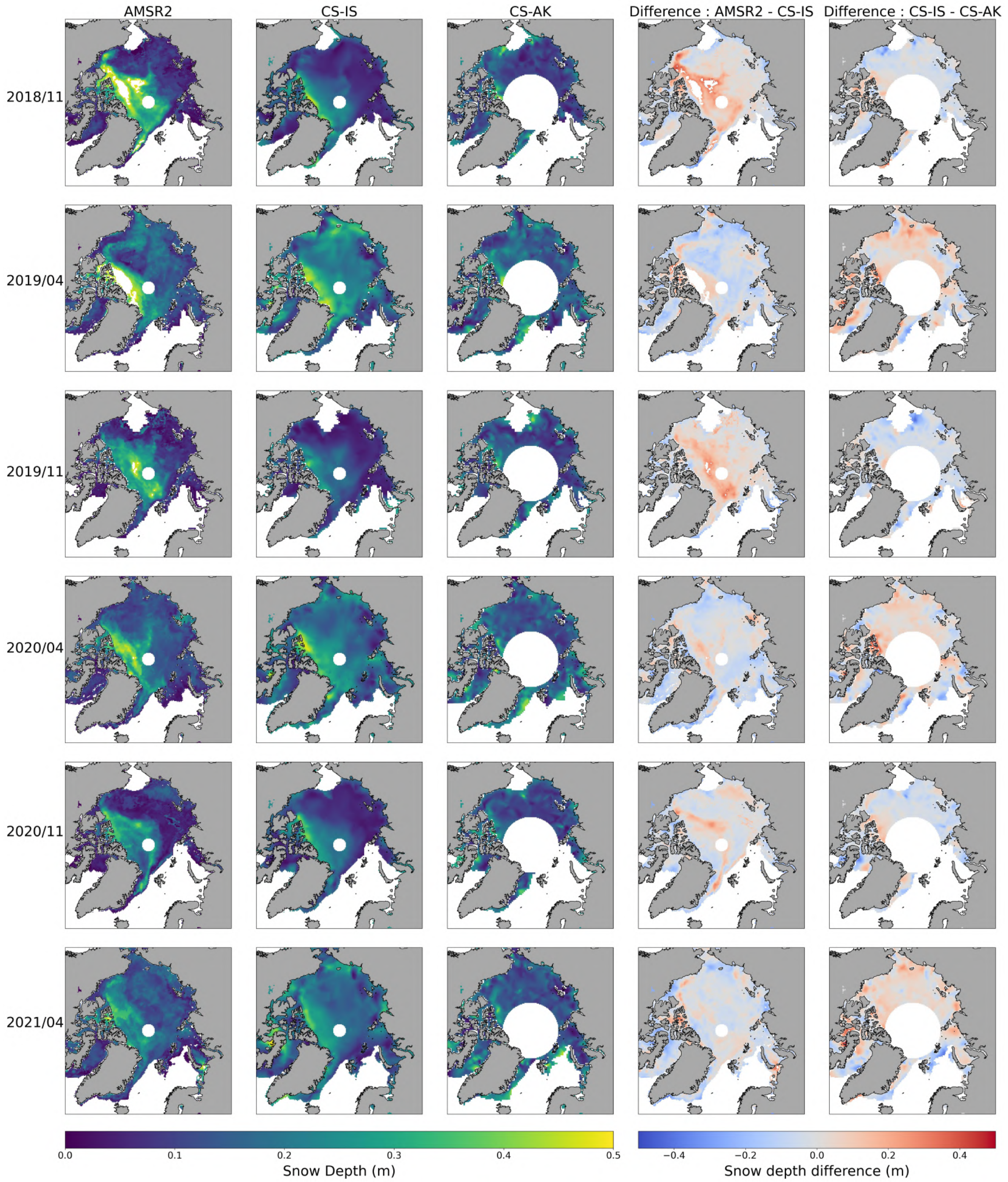

Figure 8. Comparison of our inversion for SD against AMSR2 product with $\alpha_{cs} = 1$ and $\alpha_{ak} = 0$. We also compute the difference between AMSR2 and the CS-IS combination and the difference between the two combinations of satellites.

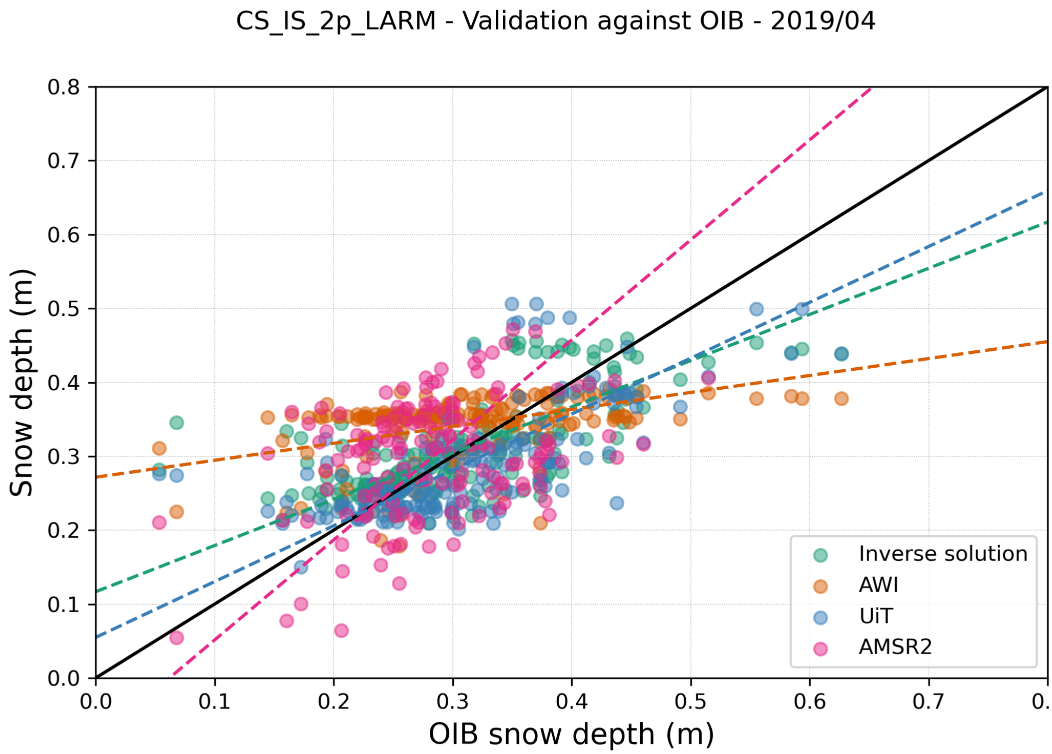

Figure 9. Evaluation of the result from the inversion using CS-IS-2p for snow depth. We compare our result with the OIB snow product, for April 2019. We also plot the snow used by AWI and the UiT and AMSR2 products.

between the inverse solution and UiT product. The SD from AWI is mainly centered around 0.35 cm for all the values plotted, which is a known issue of using the W99 climatology for MYI. Among all the datasets, AMSR2 produces the best slope and intercept, which suggests that its stronger contrast of SD between FYI and MYI zones is more realistic.

The inverse SD is furthermore evaluated against measurements from MOSAiC and IceBird campaigns (Figure 10). Similar to the comparison with OIB, the inverse solution for SD exhibits a bias and RMSE close to zero in both cases. The linear correlation coefficients obtained for these two validations are higher than those obtained when regressing against OIB. When compared to MOSAiC, the inverse solution underestimates SD by 19 cm. The derived slope (slope = 1.54) indicates that the inverse SD is underestimated for lower SD values and overestimated for higher SD values. The evaluation against IceBird yields near-perfect agreement, with a slope of 0.94. In this case, the inverse SD is overestimated by 3 cm. Overall, the statistical performance against these measurements is improved compared to the validation against OIB (Table 3, Figure 9).

4.3 Inversion for the bias factors

Moreover, the inverse approach set out in this study enables an inversion of the bias factor for one or both satellites. Figure 11a shows the results for April 2019 concerning an inversion with an unknown parameter, designated as α_{cs}, in addition to

	Inverse	AWI	UiT	AMSR2
Ice Thickness				
Bias	0.62	0.67	-	-
RMSE	0.90	0.92	-	-
r	0.67	0.60	-	-
Slope	1.29	0.99	-	-
Intercept	-0.07	0.70	-	-
Snow Depth				
Bias	0.00	0.03	-0.02	0.02
RMSE	0.07	0.09	0.07	0.09
r	0.68	0.40	0.70	0.36
Slope	0.63	0.23	0.76	1.35
Intercept	0.12	0.27	0.05	-0.08

Table 3. Computed statistics corresponding to Figure 6 and 9. The SD from AWI corresponds to the Warren Climatology. r is the linear correlation coefficient.

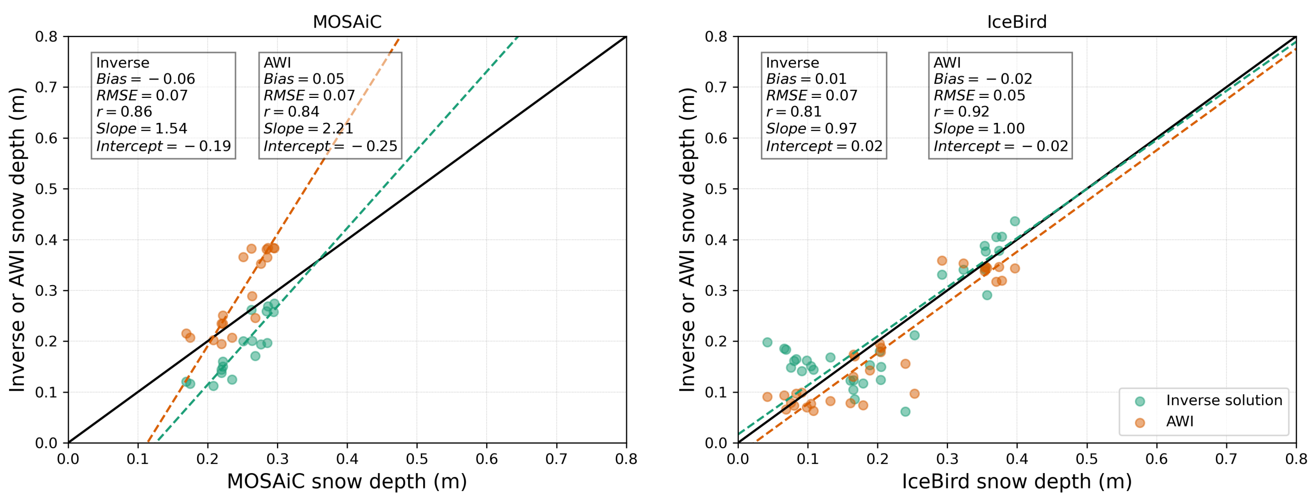

Figure 10. Evaluation of the results from the inversion using CS-IS-2p for SD. The validation is performed against MOSAiC (for Winter 2019-2020) and IceBird (for 2019/04).

SIT and SD. Figure 11b demonstrates the results for an inversion with both α_{CS} and α_{is} as unknown parameters. The findings demonstrate the efficacy of the inverse approach in generating consistent results for the bias factor (α_{cs} close to 1 and α_{is} close to 0). However, the inverse SIT and SD demonstrate a poor correlation with OIB data, emphasising the necessity for further refinement of this specific inversion. Further details on the inversions for the bias factors can be found in the Supplementary Information (Figures S5 to S13).

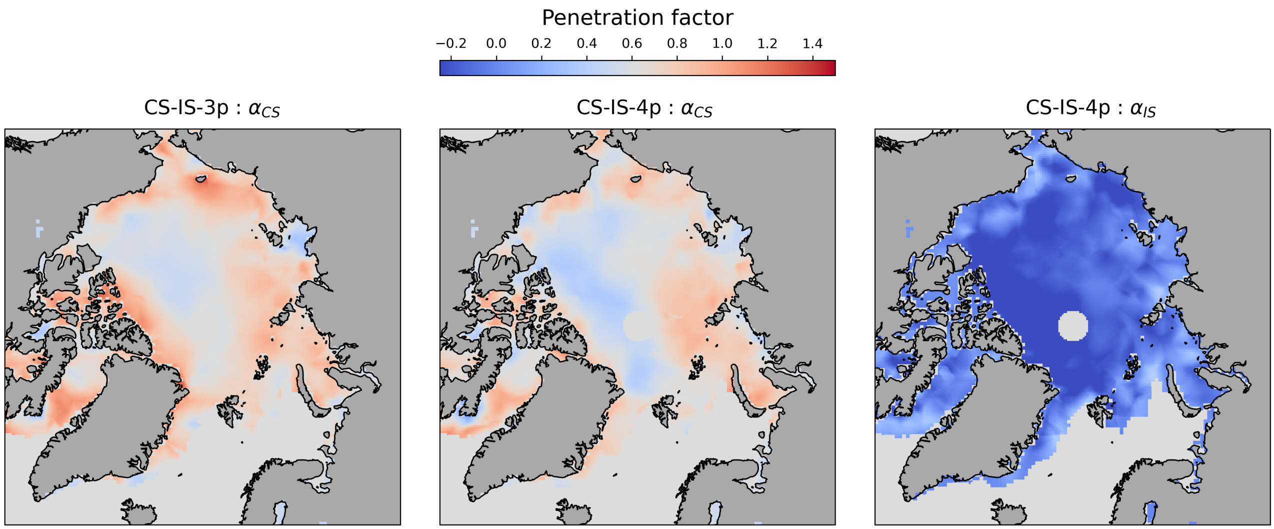

Figure 11. Result of the inversion with CS-IS-3p (inversion for SD, SIT and α_{cs}) and CS-IS-4p (inversion for SD, SIT, α_{cs} and α_{is}) for April 2019 for the bias factors. The priors on the different physical parameters can be found in Section 3.

5 Discussion

5.1 Sea ice thickness and snow depth retrievals

This study demonstrates the capability of the Bayesian approach to simultaneously retrieve SIT and SD from along-track freeboard measurements, without requiring data interpolation or coincident satellite orbits. The methodology successfully captures well-established geographical patterns in SIT and SD, including the presence of thicker ice north of Greenland and within the Canadian Archipelago, regions dominated by MYI.

The retrieved SIT and SD estimates show promising agreement with existing datasets, exhibiting consistency with AWI SIT and AMSR2 SD products. Furthermore, the results display encouraging correlations with validation data (OIB, BGEP-ULS, MOSAiC, IceBird). The inverse method's ability to capture interannual variability is particularly promising, as this is a known weakness of commonly used SIT products (Nab et al., 2024). However, a systematic bias is observed, with the inversion method underestimating SIT by 0.07 m while overestimating SD by 0.12 m relative to OIB. Several potential explanations for this bias are considered. One contributing factor may be the assumption of full radar penetration in the CryoSat-2 retrievals ($\alpha_{cs} = 1$). Differentiating the freeboard equations (Equations 3, 5) with respect to α_{cs} indicates that an increase in penetration factor ($\alpha_{cs} > 1$) would lead to higher SIT estimates. However, given that penetration factors are typically constrained within the range [0,1], a value exceeding unity would suggest scattering of the Ku-band within the ice pack, which is not physically expected. Additionally, the observed 7 cm SIT underestimation could be linked to systematic biases in the input freeboard data or the smoothing effect of the inversion approach over the OIB comparison region (left map in Figure 6). This underestimation could also be a consequence of the choice of constant values for the sea ice density. Validating the inverse SIT against the

BGEP-ULS moorings suggested that the inverse approach captured the seasonal and interannual variations in ice thickness quite well. This is particularly evident in the values of r close to 1 for the three locations.

Regarding SD retrieval, the overestimation of 0.12 m compared to OIB aligns with known biases in the OIB Quick-Look SD product, which underestimates SD by approximately 0.08 m (Kwok et al., 2017). When evaluating SD inversion performance against MOSAiC (Winter 2019-2020) and IceBird (April 2019), different trends emerge. The CS-IS-2p inversion underestimates SD by 0.19 m compared to MOSAiC. This discrepancy compared to the OIB evaluation may be attributed to temporal and regional differences, as MOSAiC measurements were conducted during Winter 2019-2020 in the central Arctic, north of Svalbard, whereas OIB data correspond to April 2019 observations with measurements made in other regions of Central Arctic. For IceBird, where the measurements were also performed during April 2019, the inversion yields an SD overestimation of 0.03 m, suggesting a closer agreement with OIB than with MOSAiC. The differences in measurement techniques and geographical coverage likely explain the varying correlation statistics observed across validation datasets (OIB, MOSAiC and IceBird).

5.2 Computation of bias factors in addition to SIT and SD

The inverse method introduced in the paper can provide probabilistic inversions even for seemingly unconstrained problems: this comes from the existence of prior information and the inherent correlation scales that are introduced in the Bayesian inversion approach. Thus, given an user-defined prior probability distribution $P(\mathbf{m})$, we can also invert for the bias factor α in addition of SIT and SD. The inversion framework estimates the bias factors for each satellite. We show some of these inversion results in Supplementary Information (Figures S5 to S13). The retrieved values align well with expected ranges for radar (Ku-band) and laser measurements, despite the use of a weakly constrained prior. Further investigation is required to refine the spatial patterns observed in the retrieved bias factor maps and their relationship with SIT and SD results. Adjustments to the prior distribution or modifications to the inversion framework may be necessary to ensure more physically consistent results.

5.3 Forward modelling

In this study, we focused on 3 satellites (CS, IS, AK) but the method could be adapted to other radar/laser altimeters and other sensors. In addition, we have only used a combination of two satellites. However, the algorithm can be easily modified to include freeboards from more than two satellites. This requires the definition of one equation per satellite (for example, we could perform the inversion with Equations 3, 4 and 5). The advantage of conducting the inversion using all three equations and satellites is that it leverages a larger dataset, enhancing the robustness of the analysis (3 data sources instead of 2). This means that we could perform the inversion using a smaller number of days of data (e.g. 7 days) and still have the same number of freeboards as if we used two satellites but 15 days of data. This allowance for satellites fusion and the multiplicity of altimeters in orbit needs to be further investigated and is promising with a view to future missions.

In an inverse problem, we need to define a forward model, described here by Equations 3, 4 and 5. A change in the forward modelling would have an impact on the inverse solution. Another idea would also be to invert for a *mass* $\frac{\rho_w - \rho_i}{\rho_w} H_i$ instead of inverting for SIT (c.f. Equation 3). This requires a choice on the prior for this new parameter. Additionally, in this study, a constant value for the snow density (ρ_s) was used. Following the methods of Mallett (2024), this value could be varied temporally, to better represent the densification of snow throughout the winter season. Similarly joint inversions of the sea ice density is also possible in principle. Given the sea ice density as a free parameter, we could define a prior distribution that includes ice age and potentially other factors as weighting. Further works on this inverse method could aim at investigating these questions.

Furthermore, while our study focuses on the Arctic, this algorithm can also be applied to estimate ice and snow thickness in the Antarctic. Additionally, the inversion can be performed over specific polar regions to enable targeted studies of particular areas with large uncertainties identified by our probabilistic inversion method.

5.4 Choice of error

The estimated error associated to the observations is an input parameter of the inversion that can be modified. Here, we presented our result with an error computed using calculated freeboard uncertainties. Another approach to this specific question would be to set up a hyper-parameter λ to scale data errors and to use a hierarchical Bayes approach, where this parameter is treated as an unknown in the inversion (Malinverno and Briggs, 2004; Hawkins et al., 2019a):

$$\sigma = \lambda\sigma_{data} \tag{11}$$

where σ is the standard deviation in Equation 10, λ the unknown hierarchical parameter and σ_{data} the error vector on the input prior to the inversion.

6 Conclusions

We have introduced a new application of a Bayesian method for retrieving ice and snow thickness in the Arctic Ocean. We showed that this innovative approach is valid for computing SIT and SD without assumptions on the SD (the main source of uncertainties). The solution is probabilistic, thus producing thousands of models and making possible further investigations on the covariances and on the joint probabilities of ice and snow depth. We showed the application of this approach on a synthetic test, in order to demonstrate its advantages compared to classical interpolation methods and to emphasise the probabilistic framework. Then, we introduced SIT and SD inverse results using real freeboard data and compared these maps against existing products (AWI, AMSR2, UiT) and independent data (BGEP, MOSAiC, IceBird, OIB) which show promising results, though further tuning of the algorithm is necessary to generate an optimized product of jointly inverted SD and SIT. This includes a better understanding of the impact of the bias factors on both SIT and SD, which are likely related to the radar waves' ability to penetrate the snow, the retracking algorithm and processing chain used to derive freeboards, and the impact of the sea ice density.

We showed that this algorithm is also able to compute maps for the bias factors of the satellites used. This could help future research into the behaviour of α and its link with SIT and SD (using the covariances for example or with more sensitivity studies). In the meantime, this will allow further investigation on temporal and spatial variability of the bias factor.

One of the main advantages of this code is that it can be extensively customised and further improved. The forward model could be refined to invert for ice mass instead of the SIT or to invert for a deviation to a background instead of looking at the absolute values of the physical parameters. The error on the input could be changed and could even be an unknown for the inversion. This list of further investigations of this method is of course not exhaustive and paves the way for future work to efficiently construct maps of sea ice and snow depth over the poles.

Code and data availability. The code used to perform the inversion and conduct the analysis can be found at https://doi.org/10.5281/zenodo.17475067. The ice type data is available at Aaboe et al. (2021). The OIB Quick-Look data is available at Kurtz et al. (2016). The gridded CS2 and AK radar freeboard data are available via Landy et al. (2024). The along-track IS2 laser freeboard data is available at Kwok et al. (2023a). The AWI and AMSR-2 SIT products are available via Hendricks et al. (2023) and Rostosky et al. (2018) respectively. MOSAiC data are available via Itkin et al. (2021) and IceBird data can be found via Jutila et al. (2021). The mooring data from the Beaufort gyre exploration project (BGEP) are retrieved from https://www2.whoi.edu/site/beaufortgyre/data/mooring-data/

Author contributions. ERB and MT led the project and the conceptualisation of the study. ERB performed the inversions. ERB wrote the paper with the help of MT, TB, CN, SSBAR, JL, HH, RW and MF. CN and JL computed the along-track binned data and calculated the uncertainties. TB and MF provided theoretical support on the application of the method. SSBAR, JPF and TS worked on the development of the method. MT, CG and HH initiated the project several years ago.

Competing interests. Some authors are members of the editorial board of The Cryosphere

Acknowledgements. MT acknowledges support from ESA (#ESA/AO/1-9132/17/NL/MP & #ESA/AO/1-10061/19/I-EF, SINX'S, CLEV2ER) and NERC (#NE/T000546/1 & #NE/X004643/1). CN acknowledges support from NERC (#NE/S007229/1), the UK Met Office (CASE Partnership) and ESA (#ESA/AO/1-10061/19/I-EF).

References

Aaboe, S., Down, E., Sørensen, A., Lavergne, T., and Eastwood, S.: Sea-ice type climate data record Oct 1978-Aug 2023, https://doi.org/10.24381/CDS.29C46D83, 2021.

Alexandrov, V., Sandven, S., Wahlin, J., and Johannessen, O. M.: The relation between sea ice thickness and freeboard in the Arctic., The Cryosphere, 4(3), https://doi.org/10.5194/tc-4-373-2010, 2010.

Armitage, T. W. and Ridout, A. L.: Arctic sea ice freeboard from AltiKa and comparison with CryoSat-2 and Operation IceBridge, Geophysical Research Letters, 42, 6724–6731, 2015.

Bodin, T. and Sambridge, M.: Seismic tomography with the reversible jump algorithm, Geophysical Journal International, 178, 1411–1436, https://doi.org/https://doi.org/10.1111/j.1365-246X.2009.04226.x, 2009.

Brodzik, M. J., Billingsley, B., Haran, T., Raup, B., and Savoie, M. H.: EASE-grid 2.0: Incremental but significant improvements for Earth-gridded data sets., ISPRS International Journal of Geo-Information, https://doi.org/https://doi.org/10.3390/ijgi1010032, 2012.

Brooks, S., Gelman, A., Jones, G., and Meng, X.-L.: Handbook of Markov Chain Monte Carlo, New York: Chapman and Hall/CRC, 2011.

Dettmering, D., Schwatke, C., and Bosch, W.: Global Calibration of SARAL/AltiKa Using Multi-Mission Sea Surface Height Crossovers, Marine Geodesy, 38, 206–218, https://doi.org/https://doi.org/10.1080/01490419.2014.988832, 2015.

Forsström, S., Gerland, S., and Pedersen, C. A.: Annals of Glaciology, 52, 261–270, 2011.

Green, P. J.: Reversible jump Markov chain Monte Carlo computation and Bayesian model determination, Biometrika, 82, 711–732, https://doi.org/https://doi.org/10.1093/biomet/82.4.711, 1995.

Gregory, W., Lawrence, I. R., and Tsamados, M.: A Bayesian approach towards daily pan-Arctic sea ice freeboard estimates from combined CryoSat-2 and Sentinel-3 satellite observations, The Cryosphere, https://doi.org/https://doi.org/10.5194/tc-15-2857-2021, 2021.

Gregory, W., Bushuk, M., Zhang, Y., Adcroft, A., and Zanna, L.: Machine Learning for Online Sea Ice Bias Correction Within Global Ice-Ocean Simulations, Geophysical Research Letters, 51, https://doi.org/https://doi.org/10.1029/2023GL106776, 2024a.

Gregory, W., MacEachern, R., Takao, S., Lawrence, I. R., Nab, C., Deisenroth, M. P., and Tsamados, M.: Scalable interpolation of satellite altimetry data with probabilistic machine learning, Nature Communications, 15, 7453, 2024b.

Guerreiro, K., Fleury, S., Zakharova, E., Rémy, F., and Kouraev, A.: Potential for estimation of snow depth on Arctic sea ice from CryoSat-2 and SARAL/AltiKa missions, Remote Sensing of Environment, 186, 339–349, https://doi.org/http://dx.doi.org/10.1016/j.rse.2016.07.013, 2016.

Hawkins, R., Bodin, T., Sambridge, M., Choblet, G., and Husson, L.: Trans-dimensional surface reconstruction with different classes of parameterization, Geochemistry, Geophysics, Geosystems, 20, 505–529, https://doi.org/https://doi.org/10.1029/2018GC008022, 2019a.

Hawkins, R., Husson, L., Choblet, G., Bodin, T., and Pfeffer, J.: Virtual tide gauges for predicting relative sea level rise, Journal of Geophysical Research: Solid Earth, 124, 13 367–13 391, https://doi.org/https://doi.org/10.1029/2019JB017943, 2019b.

Hendricks, S., Ricker, R., and Paul, S.: Product User Guide & Algorithm Specification: AWI CryoSat-2 Sea Ice Thickness (version 2.6), 2023.

Itkin, P., Webster, M., Hendricks, S., Oggier, M., Jaggi, M., Ricker, R., Arndt, S., Divine, D. V., von Albedyll, L., Raphael, I., Rohde, J., and Liston, G. E.: Magnaprobe snow and melt pond depth measurements from the 2019-2020 MOSAiC expedition, https://doi.org/10.1594/PANGAEA.937781, 2021.

Jutila, A., Hendricks, S., Ricker, R., von Albedyll, L., and Haas, C.: Airborne sea ice parameters during the IceBird Winter 2019 campaign in the Arctic Ocean, Version 1, https://doi.org/10.1594/PANGAEA.933912, 2021.

Kacimi, S. and Kwok, R.: Arctic Snow Depth, Ice Thickness, and Volume From ICESat-2 and CryoSat-2: 2018–2021, Geophysical Research Letters, 49, e2021GL097 448, https://doi.org/https://doi.org/10.1029/2021GL097448, 2022.

Kurtz, N., Studinger, M., Harbeck, J., Onana, V., and Yi, D.: IceBridge Sea Ice Freeboard, Snow Depth, and Thickness Quick Look, Version 1, https://doi.org/10.5067/GRIXZ91DE0L9, 2016.

Kwok, R.: Simulated effects of a snow layer on retrieval of CryoSat-2 sea ice freeboard, Geophysical Research Letters, 41, 5014–5020, https://doi.org/https://doi.org/10.1002/2014GL060993, 2014.

Kwok, R.: Arctic sea ice thickness, volume, and multiyear ice coverage: losses and coupled variability (1958–2018), Environmental Research Letters, 13, https://doi.org/DOI 10.1088/1748-9326/aae3ec, 2018.

Kwok, R. and Markus, T.: Potential basin-scale estimates of Arctic snow depth with sea ice freeboards from CryoSat-2 and ICESat-2: An exploratory analysis, Advances in Space Research, 62, https://doi.org/https://doi.org/10.1016/j.asr.2017.09.007, 2017.

Kwok, R. and Rothrock, D. A.: Decline in Arctic sea ice thickness from submarine and ICESat records: 1958–2008, Geophysical Research Letters, 36, https://doi.org/https://doi.org/10.1029/2009GL039035, 2009.

Kwok, R., Kurtz, N. T., Brucker, L., Ivanoff, A., Newman, T., Farrell, S. L., King, J., Howell, S., Webster, M. A., Paden, J., Leuschen, C., MacGregor, J. A., Richter-Menge, J., Harbeck, J., , and Tschudi, M.: Intercomparison of snow depth retrievals over Arctic sea ice from radar data acquired by Operation IceBridge, The Cryosphere, 11, 2571–2593, https://doi.org/https://doi.org/10.5194/tc-11-2571-2017, 2017.

Kwok, R., Kacimi, S., Webster, M., Kurtz, N., and Petty, A.: Arctic Snow Depth and Sea Ice Thickness From ICESat-2 and CryoSat-2 Freeboards: A First Examination, Journal of Geophysical Research: Oceans, 125, https://doi.org/https://doi.org/10.1029/2019JC016008, 2020.

Kwok, R., Petty, A., Cunningham, G., Markus, T., Ivanoff, D. H. A., Wimert, J., Bagnardi, M., and Kurtz, N.: ATLAS/ICESat-2 L3A Sea Ice Freeboard, Version 6, https://doi.org/10.5067/ATLAS/ATL10.006, 2023a.

Kwok, R., Petty, A. A., Cunningham, G., Markus, T., Hancock, D., I., A., W., J., B., M., K. N., and the ICESat-2 Science Team: (ATL10, Version 6), https://doi.org/https://doi.org/10.5067/ATLAS/ATL10.006, 2023b.

Landy, J. C., Petty, A. A., Tsamados, M., and Stroeve, J. C.: Sea ice roughness overlooked as a key source of uncertainty in CryoSat-2 ice freeboard retrievals, Journal of Geophysical Research: Oceans, 125, e2019JC015 820, 2020.

Landy, J. C., Dawson, G. J., Tsamados, M., Bushuk, M., Stroeve, J. C., Howell, S. E. L., Krumpen, T., Babb, D. G., Komarov, A. S., Heorton, H. D. B. S., Belter, H. J., and Aksenov, Y.: A year-round satellite sea-ice thickness record from CryoSat-2, Nature, 609, 517–522, https://doi.org/https://doi.org/10.1038/s41586-022-05058-5, 2022.

Landy, J. C., de Rijke-Thomas, C., Nab, C., Lawrence, I., Glissenaar, I. A., Mallett, R. D., Fredensborg Hansen, R. M., Petty, A., Tsamados, M., Macfarlane, A. R., et al.: Anticipating CRISTAL: An exploration of multi-frequency satellite altimeter snow depth estimates over Arctic sea ice, 2018–2023, EGUsphere, 2024, 1–41, https://doi.org/https://doi.org/10.5194/egusphere-2024-2904, 2024.

Lawrence, I. R., Tsamados, M. C., Stroeve, J. C., Armitage, T. W., and Ridout, A. L.: Estimating snow depth over Arctic sea ice from calibrated dual-frequency radar freeboards, The Cryosphere, 12, 3551–3564, https://doi.org/https://doi.org/10.5194/tc-12-3551-2018, 2018.

Laxon, S., Peacock, N., and Smith, D.: High interannual variability of sea ice thickness in the Arctic region, Nature, https://doi.org/https://doi.org/10.1038/nature02050, 2003.

Malinverno, A. and Briggs, V. A.: Expanded uncertainty quantification in inverse problems: Hierarchical Bayes and empirical Bayes, Geophysics, 69, https://doi.org/https://doi.org/10.1190/1.1778243, 2004.

Mallett, R.: A methodologically robust seasonal snow densification function from Soviet North Pole drifting station data, Manuscript submitted for publication, 2024.

Mallett, R. D., Lawrence, I. R., Stroeve, J. C., Landy, J. C., and Tsamados, M.: Brief communication: Conventional assumptions involving the speed of radar waves in snow introduce systematic underestimates to sea ice thickness and seasonal growth rate estimates, The Cryosphere, 14, 251–260, https://doi.org/10.5194/tc-14-251-2020, 2020.

Nab, C., Mallett, R., Gregory, W., Landy, J., Lawrence, I., Willatt, R., Stroeve, J., and Tsamados, M.: Synoptic variability in satellite altimeter-derived radar freeboard of Arctic sea ice, Geophysical Research Letters, 50, e2022GL100 696, https://doi.org/10.1029/2022GL100696, 2023.

Nab, C., Mallett, R., Nelson, C., Stroeve, J., and Tsamados, M.: Optimising interannual sea ice thickness variability retrieved from CryoSat-2, Geophysical Research Letters, 51, e2024GL111 071, 2024.

Nab, C., Mignac, D., Landy, J., Martin, M., Stroeve, J., and Tsamados, M.: Sensitivity to sea ice thickness parameters in a coupled ice-ocean data assimilation system, Journal of Advances in Modeling Earth Systems, https://doi.org/10.1029/2024MS004276, 2025.

Nandan, V., Geldsetzer, T., Yackel, J., Mahmud, M., Scharien, R., Howell, S., King, J., Ricker, R., and Else, B.: Effect of Snow Salinity on CryoSat-2 Arctic First-Year Sea Ice Freeboard Measurements, Geophysical Research Letters, 44, https://doi.org/10.1002/2017GL074506, 2017.

Nicolaus, M., Perovich, D. K., Spreen, G., Granskog, M. A., von Albedyll, L., Angelopoulos, M., Anhaus, P., Arndt, S., Belter, H. J., Bessonov, V., Birnbaum, G., Brauchle, J., Calmer, R., Cardellach, E., Cheng, B., Clemens-Sewall, D., Dadic, R., Damm, E., de Boer, G., Demir, O., Dethloff, K., Divine, D. V., Fong, A. A., Fons, S., Frey, M. M., Fuchs, N., Gabarró, C., Gerland, S., Goessling, H. F., Gradinger, R., Haapala, J., Haas, C., Hamilton, J., Hannula, H.-R., Hendricks, S., Herber, A., Heuzé, C., Hoppmann, M., Høyland, K. V., Huntemann, M., Hutchings, J. K., Hwang, B., Itkin, P., Jacobi, H.-W., Jaggi, M., Jutila, A., Kaleschke, L., Katlein, C., Kolabutin, N., Krampe, D., Kristensen, S. S., Krumpen, T., Kurtz, N., Lampert, A., Lange, B. A., Lei, R., Light, B., Linhardt, F., Liston, G. E., Loose, B., Macfarlane, A. R., Mahmud, M., Matero, I. O., Maus, S., Morgenstern, A., Naderpour, R., Nandan, V., Niubom, A., Oggier, M., Oppelt, N., Pätzold, F., Perron, C., Petrovsky, T., Pirazzini, R., Polashenski, C., Rabe, B., Raphael, I. A., Regnery, J., Rex, M., Ricker, R., Riemann-Campe, K., Rinke, A., Rohde, J., Salganik, E., Scharien, R. K., Schiller, M., Schneebeli, M., Semmling, M., Shimanchuk, E., Shupe, M. D., Smith, M. M., Smolyanitsky, V., Sokolov, V., Stanton, T., Stroeve, J., Thielke, L., Timofeeva, A., Tonboe, R. T., Tavri, A., Tsamados, M., Wagner, D. N., Watkins, D., Webster, M., and Wendisch, M.: Overview of the MOSAiC expedition: Snow and sea ice, Elementa: Science of the Anthropocene, 10, 000 046, https://doi.org/10.1525/elementa.2021.000046, 2022.

Oelsmann, J., Marcos, M., Passaro, M., Sanchez, L., Dettmering, D., Dangendorf, S., and Seitz, F.: Regional variations in relative sea-level changes influenced by nonlinear vertical land motion, Nature Geoscience, 17, 137–144, https://doi.org/https://doi.org/10.1038/s41561-023-01357-2, 2024.

Petty, A. A., Keeney, N., Cabaj, A., Kushner, P., and Bagnardi, M.: Winter Arctic sea ice thickness from ICESat-2: upgrades to freeboard and snow loading estimates and an assessment of the first three winters of data collection, The Cryosphere, 17, 127–156, https://doi.org/https://doi.org/10.5194/tc-17-127-2023, 2023.

Pörtner, H.-O., Roberts, D., Masson-Delmotte, V., Zhai, P., Tignor, M., Poloczanska, E., Mintenbeck, K., Alegría, A., Nicolai, M., Okem, A., Petzold, J., Rama, B., and Weyer, N.: Summary for Policymakers, IPCC Special Report on the Ocean and Cryosphere in a Changing Climate, 2019.

Rostosky, P., Spreen, G., Farrell, S. L., Frost, T., Heygster, G., and Melsheimer, C.: Snow Depth Retrieval on Arctic Sea Ice From Passive Microwave Radiometers—Improvements and Extensions to Multiyear Ice Using Lower Frequencies, Journal of Geophysical Research: Oceans, 123, https://doi.org/https://doi.org/10.1029/2018JC014028, 2018.

Rothrock, D. A., Zhang, J., and Yu, Y.: The arctic ice thickness anomaly of the 1990s: A consistent view from observations and models, Journal of Geophysical Research: Oceans, 108, https://doi.org/https://doi.org/10.1029/2001JC001208, 2003.

Sambridge, M., Braun, J., and McQueen, H.: Geophysical parametrization and interpolation of irregular data using natural neighbours, Geophysical Journal International, 122, https://doi.org/https://doi.org/10.1111/j.1365-246X.1995.tb06841.x, 1995.

Shi, H., Sohn, B.-J., Dybkjær, G., Tonboe, R. T., and Lee, S.-M.: Simultaneous estimation of wintertime sea ice thickness and snow depth from space-borne freeboard measurements, The Cryosphere, https://doi.org/https://doi.org/10.5194/tc-14-3761-2020, 2020.

Stroeve, J. and Notz, D.: Changing state of Arctic sea ice across all seasons, Environmental Research Letters, 13, 103 001, https://doi.org/10.1088/1748-9326/aade56, 2018.

Tarantola, A.: Inverse problem theory and methods for model parameter estimation, 2005.

Tilling, R. L., Ridout, A., and Shepherd, A.: Estimating Arctic sea ice thickness and volume using CryoSat-2 radar altimeter data., Advances in Space Research, 62, https://doi.org/https://doi.org/10.1016/j.asr.2017.10.051, 2018.

Wadhams, P., Tucker, W. B., Krabill, W. B., Swift, R. N., Comiso, J. C., and Davis, N. R.: Relationship Between Sea Ice Freeboard and Draft in the Arctic Basin, and Implications for Ice Thickness Monitoring, Journal of Geophysical Research, 97, https://doi.org/https://doi.org/10.1029/92JC02014, 1992.

Warren, S. G., Rigor, I. G., Untersteiner, N., Radionov, V. F., Bryazgin, N. N., Aleksandrov, Y. I., and Colony, R.: Snow Depth on Arctic Sea Ice, Journal of Climate, 12, 1814 – 1829, https://doi.org/10.1175/15200442(1999)012<1814:SDOASI>2.0.CO;2, 1999.

Webster, M. A., Rigor, I. G., Nghiem, S. V., Kurtz, N. T., Farrell, S. L., Perovich, D. K., and Sturm, M.: Interdecadal changes in snow depth on Arctic sea ice, Journal of Geophysical Research : Oceans, https://doi.org/10.1002/2014JC009985, 2014.

Willatt, R., Laxon, S., Giles, K., Cullen, R., Haas, C., and Helm, V.: Ku-band radar penetration into snow cover on Arctic sea ice using airborne data, Annals of Glaciology, https://doi.org/10.3189/172756411795931589, 2011.

Willatt, R., Stroeve, J. C., Nandan, V., Newman, T., Mallett, R., Hendricks, S., Ricker, R., Mead, J., Itkin, P., Tonboe, R., Wagner, D. N., Spreen, G., Liston, G., Schneebeli, M., Krampe, D., Tsamados, M., Demir, O., Wilkinson, J., Jaggi, M., Zhou, L., Huntemann, M., Raphael, I. A., Jutila, A., and Oggier, M.: Retrieval of Snow Depth on Arctic Sea Ice From Surface-Based, Polarimetric, Dual-Frequency Radar Altimetry, Geophysical Research Letters, https://doi.org/https://doi.org/10.1029/2023GL104461, 2023.

Wingham, D. J., Francis, C. R., Baker, S. Bouzinac, C., Brockley, D., Cullen, R., De Chateau-Thierry, P., Laxon, S. W., Mallow, U., Mavrocordatos, C., Phalippou, L., Ratier, G., Rey, L., Rostan, F., Viau, P., and Wallis, D. W.: CryoSat: A mission to determine the fluctuations in Earth's land and marine ice fields, Advances in Space Research, 37, 841–871, https://doi.org/https://doi.org/10.1016/j.asr.2005.07.027, 2006.

Zygmuntowska, M., Rampal, P., Ivanova, N., and Smedsrud, L. H.: Uncertainties in Arctic sea ice thickness and volume: new estimates and implications for trends, The Cryosphere, 8, 705–720, https://doi.org/https://doi.org/10.5194/tc-8-705-2014, 2014.